*J. Fluid Mech.* (2006), *vol.* 567, *pp.* 185–194. © 2006 Cambridge University Press 
doi:10.1017/S0022112006002266 Printed in the United Kingdom

# Wake-induced forces and torques on a zigzagging/spiralling bubble

By GUILLAUME MOUGIN† AND JACQUES MAGNAUDET

Institut de Mécanique des Fluides de Toulouse, UMR CNRS/INPT/UPS 5502,
Allée Camille Soula, 31400 Toulouse, France

(Received 14 June 2006 and in revised form 28 July 2006)

The numerical results obtained by Mougin & Magnaudet (*Phys. Rev. Lett.* vol. 88, 2002*a*, 14502) for the flow past a freely moving spheroidal bubble with a prescribed spheroidal shape are processed to analyse the evolution of the forces and torques experienced by the bubble when it rises along a planar zigzag and a circular helix. It is found that, as soon as the wake becomes three-dimensional, a lateral force with a strength comparable with that of the buoyancy force occurs. This force, together with the corresponding torque, drives the horizontal movements of the bubble. The force and torque balances reveal how these wake-induced effects are balanced by added-mass effects to make possible the existence of zigzag and helical motions along which the angle between the velocity and the symmetry axis of the bubble remains small. The evolution of the wake during the zigzag indicates that the sign of the trailing vortices, and thus that of the wake-induced force and torque, is governed by the rotation of the bubble and reveals the sensitivity of the wake dynamics to the changes in the bubble velocity and rotation rate.

## 1. Introduction

Path instability of millimetric bubbles rising in water has attracted attention for a long time (Prosperetti *et al.* 2003). However the origin of this phenomenon remained uncertain until recently. An overview of experimental and theoretical investigations of this problem during the second half of the last century is given by Magnaudet & Eames (2000). Removing several possible causes of path instability, such as shape oscillations or contamination by surfactants, Mougin & Magnaudet (2002*a*, hereinafter referred to as MM) achieved a full numerical determination of the path of an oblate bubble with a prescribed shape rising freely in a slightly viscous Newtonian fluid. They showed that wake instability is the primary cause of path instability. In particular they observed that, as soon as two counter-rotating trailing vortices appear behind the bubble, its path changes from rectilinear to zigzag. Based on that numerical study, the present paper focuses on a description of the forces and torques experienced by the bubble along its path. Achieving an equivalent determination of forces and torques through a laboratory experiment is very challenging; only partial answers have yet been provided (Ellingsen & Risso 2001), as such a determination requires all components of the translational and rotational velocities of the bubble centroid to be known along the whole path. In addition to providing accurate force and torque

† Present address: L'Air Liquide, Centre de Recherche Claude Delorme 78354 Jouy en Josas, France.

estimates, the goal of the present investigation is also to obtain some insight into the way the kinematic characteristics of the bubble motion influence wake-induced effects. More precisely, as we allow for the feedback of the wake on the bubble motion, we can observe how the changes in the translational and rotational bubble velocities affect the wake dynamics, in contrast to the case of a fixed body. This in turn raises questions concerning the way the sensitivity of these dynamics to the body kinematics can be taken into account in simple models.

## 2. Numerical determination of the hydrodynamic forces and torques

The numerical approach followed by MM (thoroughly described in Mougin & Magnaudet 2002*b*) to determine the path of a freely moving bubble consisted in solving in a coupled manner the Navier–Stokes equations for the induced-flow field and the force and torque balances expressing Newton's second law for the bubble. It is well-established that when a fixed-shape body accelerates in an incompressible, time-dependent viscous flow, the hydrodynamic effects on it due to the instantaneous acceleration it communicates to the surrounding fluid (commonly referred to as added-mass effects) only depend on the geometry and instantaneous relative acceleration of the body, not on the flow characteristics (Wu 1981; Quartapelle & Napolitano 1983; Howe 1995). This key result, which for a sphere reduces to the fact that the added-mass coefficient equals 1/2, whatever the flow Reynolds number, acceleration strength, and nature of the dynamic boundary condition at the body surface (e.g. no-slip or stress-free) (Magnaudet & Eames 2000; Mougin & Magnaudet 2002*b*), may be used to separate added-mass effects from forces and torques due to vorticity (hereinafter termed 'vortical' forces and torques). More precisely, since the components of the added-mass tensor are unaffected by viscous effects, they can be evaluated from irrotational flow theory (Lamb 1945). Therefrom, the Kirchhoff–Kelvin equations which govern the general motion of a rigid body in an inviscid fluid at rest at infinity can easily be generalized to a viscous flow (Howe 1995). In the case of a body characterized by a mass $m$, an inertia tensor $\mathbb{J}$ and a volume $\vartheta$ and having three perpendicular symmetry planes, such as a spheroid, these equations may be written in the form

$$(m\mathbb{I}+\mathbb{A})\cdot\frac{\mathrm{d}\boldsymbol{U}}{\mathrm{d}t}+\boldsymbol{\Omega}\times((m\mathbb{I}+\mathbb{A})\cdot\boldsymbol{U})=\boldsymbol{F}_{\omega}+(m-\rho\vartheta)\boldsymbol{g}, \tag{2.1a}$$

$$(\mathbb{J}+\mathbb{D})\cdot\frac{\mathrm{d}\boldsymbol{\Omega}}{\mathrm{d}t}+\boldsymbol{\Omega}\times((\mathbb{J}+\mathbb{D})\cdot\boldsymbol{\Omega})+\boldsymbol{U}\times(\mathbb{A}\cdot\boldsymbol{U})=\boldsymbol{\Gamma}_{\omega}, \tag{2.1b}$$

where $\mathbb{A}$ and $\mathbb{D}$ are the symmetric translational and rotational added-mass tensors, respectively, $\mathbb{I}$ is the unit tensor, $\boldsymbol{F}_{\omega}$ and $\boldsymbol{\Gamma}_{\omega}$ are the vortical force and torque acting on the body, respectively, $\boldsymbol{g}$ is the gravity vector and $\rho$ is the fluid density which we assume to be uniform (like the body density). Equations (2.1) are written in a coordinate system having its origin fixed in the laboratory frame and its axes parallel at each instant to axes attached to the body, so that $\mathbb{A}$ and $\mathbb{D}$ do not depend on time and the body translational and rotational velocities $\boldsymbol{U}$ and $\boldsymbol{\Omega}$ are those measured by a fixed observer but with components projected onto axes rotating with the body. Note that $\boldsymbol{F}_{\omega}$ and $\boldsymbol{\Gamma}_{\omega}$ contain all the effects due to the existence of vorticity in the flow, including possible history effects.

To obtain the various terms in (2.1), MM solved the Navier–Stokes equations for the incompressible body-induced flow, using the same rotating system of axes with origin fixed in the laboratory frame. The corresponding form of the Navier–Stokes

equations is (Mougin & Magnaudet 2002*b*)

$$\frac{\partial \boldsymbol{V}}{\partial t} + \boldsymbol{\Omega} \times \boldsymbol{V} + (\boldsymbol{V} - \boldsymbol{W}) \cdot \nabla \boldsymbol{V} = \nabla \cdot \boldsymbol{\Sigma}, \quad \nabla \cdot \boldsymbol{V} = 0, \tag{2.2}$$

where $\boldsymbol{W} = \boldsymbol{U} + \boldsymbol{\Omega} \times \boldsymbol{r}$ is the velocity of a geometrical point located at a distance $\boldsymbol{r}$ from the body centre and $\boldsymbol{\Sigma} = -(P/\rho)\mathbb{I} + \nu(\nabla \boldsymbol{V} +^t \nabla \boldsymbol{V})$ is the stress tensor of the corresponding flow ($\nu$ is the kinematic viscosity), $P$ and $\boldsymbol{V}$ being the local pressure and velocity, respectively. In the case where the body is a fixed-shaped bubble moving in a pure liquid, the appropriate boundary conditions express impermeability and zero surface shear stress, so that the flow at the body surface obeys

$$\boldsymbol{V} \cdot \boldsymbol{n} = \boldsymbol{W} \cdot \boldsymbol{n}, \quad \boldsymbol{n} \times ((\nabla \boldsymbol{V} +^t \nabla \boldsymbol{V}) \cdot \boldsymbol{n}) = \boldsymbol{0}, \tag{2.3}$$

where $\boldsymbol{n}$ is the outer unit normal to the bubble surface $\mathscr{S}$. The velocity disturbance vanishes far away from the bubble, so that $\boldsymbol{V} \to \boldsymbol{0}$ for $\|\boldsymbol{r}\| \to \infty$. After each time step, the stress tensor $\boldsymbol{\Sigma}$ has to be integrated over the bubble surface to obtain the hydrodynamic force $\boldsymbol{F}$ and torque $\boldsymbol{\Gamma}$, respectively defined by

$$\boldsymbol{F} = \int_{\mathscr{S}} \boldsymbol{\Sigma} \cdot \boldsymbol{n} \, \mathrm{d}\mathscr{S}, \quad \boldsymbol{\Gamma} = \int_{\mathscr{S}} \boldsymbol{r} \times (\boldsymbol{\Sigma} \cdot \boldsymbol{n}) \, \mathrm{d}\mathscr{S}. \tag{2.4}$$

In the computational strategy developed by Mougin & Magnaudet (2002*b*), $\boldsymbol{V}$ and $\boldsymbol{\Omega}$ are kept constant within each time step of the resolution of (2.2)–(2.3), which results in $\boldsymbol{F}$ and $\boldsymbol{\Gamma}$ containing (through the pressure $P$) all 'quasi-steady' hydrodynamic contributions but not accounting for the impulsive effects of the time rate-of-change terms $\mathrm{d}\boldsymbol{U}/\mathrm{d}t$ and $\mathrm{d}\boldsymbol{\Omega}/\mathrm{d}t$. Therefore, knowing $\boldsymbol{F}$ and $\boldsymbol{\Gamma}$ from (2.4), the generalized Kirchhoff–Kelvin equations (2.1) are solved in the form

$$(m\mathbb{I} + \mathbb{A}) \cdot \frac{\mathrm{d}\boldsymbol{U}}{\mathrm{d}t} + m\boldsymbol{\Omega} \times \boldsymbol{U} = \boldsymbol{F} + (m - \rho\vartheta)\boldsymbol{g}, \tag{2.5a}$$

$$(\mathbb{J} + \mathbb{D}) \cdot \frac{\mathrm{d}\boldsymbol{\Omega}}{\mathrm{d}t} + \boldsymbol{\Omega} \times (\mathbb{J} \cdot \boldsymbol{\Omega}) = \boldsymbol{\Gamma}. \tag{2.5b}$$

The numerical treatment of (2.2)–(2.5) is described by Mougin & Magnaudet (2002*b*), including various test cases and an analysis of the time accuracy of the complete integration algorithm.

Results discussed below were obtained by assuming that the bubble has negligible inertia compared to the surrounding liquid, which results in $m = 0$ and $\mathbb{J} = 0$ in (2.5), implying that the total hydrodynamic force and torque acting on the bubble are zero at all time. For an oblate spheroid, $\mathbb{A}$ (resp. $\mathbb{D}$) is diagonal if the axes of the coordinate system are chosen parallel to the principal axes of the body, and only has two (resp. one) independent non-zero components which may easily be evaluated (Lamb 1945) as a function of the body equivalent radius $R_{eq} = (3\vartheta/4\pi)^{1/3}$ and aspect ratio $\chi = b/a$, $a$ and $b$ denoting the minor and major semi-axes, respectively ($\vartheta = \frac{4}{3}\pi a b^2$). Owing to the rotational symmetry of the body, the time rate-of-change term in (2.5*b*) vanishes in the direction $x$ parallel to the symmetry axis. Moreover, since the shear-free condition in (2.3) implies that $\boldsymbol{\Sigma} \cdot \boldsymbol{n}$ is parallel to $\boldsymbol{n}$ at any point on the bubble surface, the $x$-component of the torque $\boldsymbol{\Gamma}$ is also zero. Therefore it turns out that the $x$-component of $\boldsymbol{\Omega}$ is immaterial and can be set to zero without loss of generality. This choice, combined with the rotational symmetry of $\mathbb{D}$ about the $x$-axis makes all three components of the term $\boldsymbol{\Omega} \times (\mathbb{D} \cdot \boldsymbol{\Omega})$ in (2.1*b*) vanish identically. Other individual 'quasi-steady' added-mass contributions $\boldsymbol{\Omega} \times (\mathbb{A} \cdot \boldsymbol{U})$ in (2.1*a*) and $\boldsymbol{U} \times (\mathbb{A} \cdot \boldsymbol{U})$ in (2.1*b*) were evaluated by using values of $\boldsymbol{U}$ and $\boldsymbol{\Omega}$ at the corresponding time step. Therefrom,

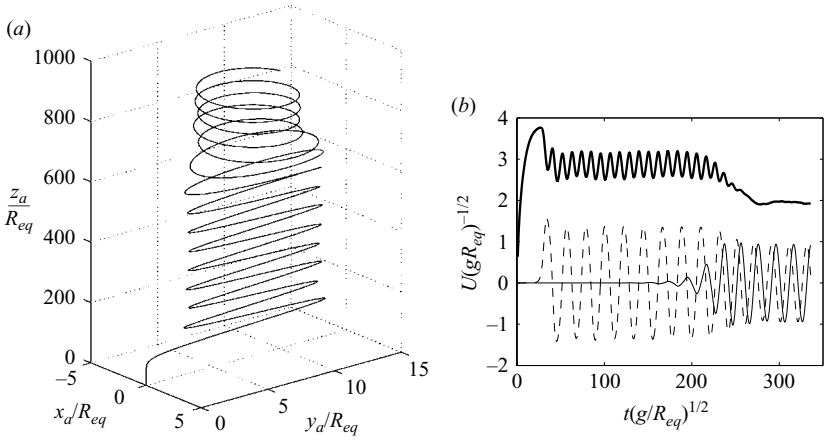


FIGURE 1. Path characteristics of an oblate bubble with $\chi = 2.50$ and $Ga = 138$ rising from rest. (*a*) Position of the bubble centroid as a function of time (horizontal scales have been magnified to make the characteristics of the zigzag and helical stages more apparent); (*b*) evolution of the vertical (thick line) and horizontal velocity components of the bubble centroid (dashed line: $y_a$-component; thin line: $z_a$-component; $(x_a, y_a, z_a)$ denotes a fixed system of axes).

the vortical force $\boldsymbol{F}_\omega$ (resp. torque $\boldsymbol{\Gamma}_\omega$) was obtained by noting that the difference between (2.1) and (2.5) implies $\boldsymbol{F}_\omega = \boldsymbol{F} + \boldsymbol{\Omega} \times (\mathbb{A} \cdot \boldsymbol{U})$ (resp. $\boldsymbol{\Gamma}_\omega = \boldsymbol{\Gamma} + \boldsymbol{U} \times (\mathbb{A} \cdot \boldsymbol{U})$).

## 3. Evolution of the forces and torques along the path

### 3.1. *Preliminary considerations*

MM detailed the evolution of the path and wake of an oblate bubble with a fixed aspect ratio $\chi = 2.5$, and a Galileo number $Ga = (gR_{eq}^3)^{1/2}/\nu = 138$ corresponding to an air bubble with an equivalent radius $R_{eq} = 1.25\,\mathrm{mm}$ rising in water under standard conditions. The corresponding trajectory is reproduced in figure 1 together with the evolution of the three velocity components of the bubble centroid. According to figure 1, the bubble successively follows a straight path, a planar zigzag and eventually a helical path. The first bifurcation of the system corresponds to a breaking of the axial symmetry of the initial wake, as also reported for a freely moving rigid sphere (Jenny, Dusek & Bouchet 2004). Similar to the case of a fixed oblate bubble, the subsequent three-dimensional wake structure, essentially made up of two counter-rotating vortices, still preserves a symmetry with respect to a plane perpendicular to that of the vortices and containing the symmetry axis of the bubble (see Magnaudet & Mougin 2006 for a detailed discussion on the origin of this primary instability). This is why during its first stage the non-rectilinear path of the bubble remains in a plane. In contrast, the second bifurcation which marks the onset of the zigzag/helix transition, corresponds to a breaking of this planar symmetry: the two vortices wrap around one another, allowing the trajectory to become three-dimensional. During the zigzag and the helical stages, the magnitude of the horizontal velocity is of the order of the gravitational velocity $(gR_{eq})^{1/2}$ (figure 1). The dimensionless frequency of the zigzag $f(R_{eq}/g)^{1/2}$ is about 0.045 while that of the helix is about 0.055, which for a real bubble corresponds to $f \approx 4.0\,\mathrm{Hz}$ and $f \approx 4.9\,\mathrm{Hz}$, respectively. Here we focus on the same case to analyse the evolution of the various contributions to the force and torque along the bubble path.

To discuss this evolution, we use a right-handed system of axes $(x, y, z)$ in which $x$ is parallel to the instantaneous direction of the minor axis of the bubble which is initially

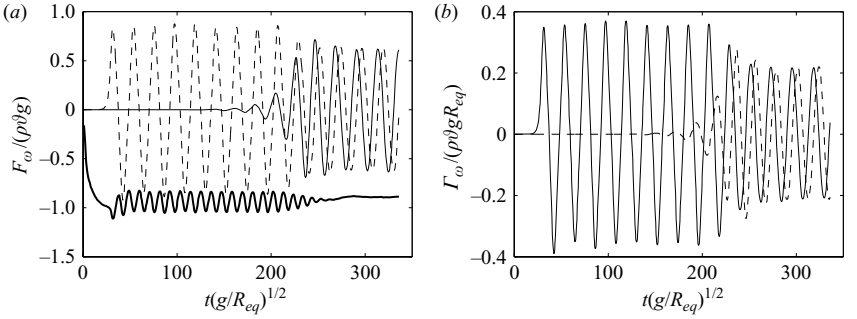


FIGURE 2. Evolution of the components of $\boldsymbol{F}_\omega$ and $\boldsymbol{\Gamma}_\omega$. Thick line: $x$-component; dashed line: $y$-component; thin line: $z$-component.

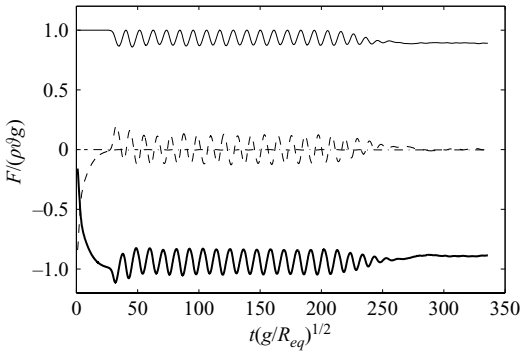


FIGURE 3. Force balance in the streamwise direction. Thick line: $F_{\omega x}$; thin line: $-\rho\vartheta g_x$; dashed line: $-[\mathbb{A}\cdot \mathrm{d}\boldsymbol{U}/\mathrm{d}t]_x$; dashed-dotted line: $-[\boldsymbol{\Omega}\times(\mathbb{A}\cdot\boldsymbol{U})]_x$.

vertical. Obviously the initial choice of $y$ and $z$ is arbitrary. Since path instability is triggered by imposing initially a small horizontal sinusoidal disturbance onto the gravity vector, the direction of this disturbance is taken as $y$; this is why the zigzag later is in the $(x, y)$-plane. Then the $y$ and $z$ axes evolve according to the condition $\Omega_x = 0$. The evolution of the three components of the vortical force $\boldsymbol{F}_\omega$ (normalized by the buoyancy force $\rho g\vartheta$) and of the two non-zero components of the vortical torque $\boldsymbol{\Gamma}_\omega$ (normalized by $\rho g R_{eq}\vartheta$) are plotted in figure 2. During the rectilinear stage ($t(g/R_{eq})^{1/2} < 25$, approximately), the vortical torque is zero and the only non-zero component of $\boldsymbol{F}_\omega$ is $F_{\omega x}$ which corresponds to a viscous drag force. As shown by figure 3, this force increases from zero since the bubble starts from rest and the constant buoyancy force is balanced by the sum of $F_{\omega x}$ and the added-mass contribution $-[\mathbb{A}\cdot \mathrm{d}\boldsymbol{U}/\mathrm{d}t]_x$. The onset of the zigzag provoked by the wake instability coincides with the occurrence of a non-zero transverse component $F_{\omega y}$ and of a torque $\Gamma_{\omega z}$. During the zigzag, $F_{\omega y}$ changes sign every half-period and reaches maximum values of about 0.85 times the buoyancy force. This is a remarkable feature, as it shows that the two counter-rotating vortices which result from the wake instability are capable of generating a force whose magnitude is comparable with that of the external driving force. We note that the oscillations of $F_{\omega x}$ have a much smaller amplitude, typically 10 % of the buoyancy force. Their frequency is twice that of $F_{\omega y}$ and $\Gamma_{\omega z}$ merely because the latter two quantities change sign every half-period of the zigzag, while $F_{\omega x}$ reaches a maximum at each extremity of the zigzag. We also note from figure 3 that, owing to the time variations of $U_x$, the streamwise added-mass contribution remains significant during the zigzag, being typically about 13 % of the buoyancy force.

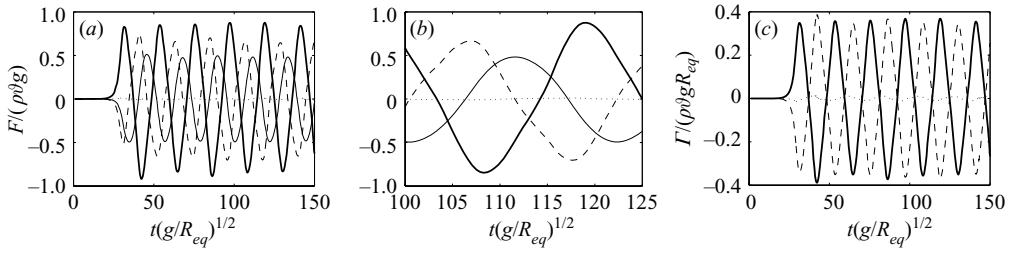


FIGURE 4. Force and torque balances in the transverse directions during the zigzag. (*a*) Force balance in the *y*-direction. (*b*) Detail of the force balance during one period (thick line: $F_{\omega y}$; thin line: $-\rho\vartheta g_y$; dashed line: $-\Omega_z(\mathbb{A}\cdot\boldsymbol{U})_x$; dotted line: $-[\mathbb{A}\cdot\mathrm{d}\boldsymbol{U}/\mathrm{d}t]_y$). (*c*) Torque balance in the *z*-direction (thick line: $\Gamma_{\omega z}$; dashed line: $U_y(\mathbb{A}\cdot\boldsymbol{U})_x - U_x(\mathbb{A}\cdot\boldsymbol{U})_y$; dotted line: $-[\mathbb{D}\cdot\mathrm{d}\boldsymbol{\Omega}/\mathrm{d}t]_z$).

During the zigzag/helix transition, the magnitude of the vortical force (resp. torque) decreases by about 25 % (resp. 40 %). This is consistent with the evolution of the horizontal displacements of the bubble displayed in figure 1 where it is seen that the amplitude of these crest-to-crest displacements decreases from $9.6R_{eq}$ during the zigzag to $6.2R_{eq}$ during the helical motion. Once the helical motion is established, the bubble reaches a constant rise velocity and $F_{\omega x}$ keeps a constant value which balances the streamwise buoyancy contribution (see figure 3). With the choice we made for the definition of the $y$ and $z$ axes, the corresponding components of $\boldsymbol{F}_\omega$ and $\boldsymbol{\Gamma}_\omega$ oscillate in time. However figure 2 clearly indicates that these components are 90° out of phase, so that $F_{\omega y}^2 + F_{\omega z}^2$ and $\Gamma_{\omega y}^2 + \Gamma_{\omega z}^2$ are constant. In other words, there is another system of rotating axes $(x, y', z')$ in which the transverse components of the force and torque appear stationary, in agreement with the observation of MM that during the helical stage the wake structure is stationary in the reference frame that rotates 'naturally' with the bubble along its helical trajectory (see also figure 8 below). Noting that for a fixed observer the bubble rotates at a rate $\omega$ about the vertical axis and rises with a constant pitch angle $\theta$ when it describes a perfect circular helix, it may be shown that this second system of axes, in which $z'$ is such that the $(x, z')$-plane contains the gravity vector and $y'$ is horizontal and perpendicular to the path, simply differs from the first one by a rotation at a rate $\omega\cos\theta$ about the $x$-axis. The latter system of axes will be used below, as it makes the comparison with the planar zigzag easier since the only non-zero component of $\boldsymbol{\Omega}$ is $\Omega_{z'}$. Note that the shape of the three successive stages of the bubble path can also be characterized by considering the evolution of $\|\boldsymbol{\Gamma}_\omega\|$ and $\|\boldsymbol{F}_\omega\cdot\boldsymbol{\Gamma}_\omega\|$: while both are zero when the path is straight, only the second is zero during the zigzag and they are eventually both non-zero during the helical stage.

### 3.2. *Force and torque balances in the transverse directions*

The various contributions to the force (resp. torque) balance along the $y$- (resp. $z$-) direction during the zigzag stage are plotted in figure 4. In addition to $F_{\omega y}$, this lateral force balance involves the centripetal added-mass contribution $-\Omega_z(\mathbb{A}\cdot\boldsymbol{U})_x$ which opposes the bubble acceleration normal to the path, the transverse added-mass contribution $-[\mathbb{A}\cdot\mathrm{d}\boldsymbol{U}/\mathrm{d}t]_y$ which opposes the time variations of the lateral velocity component $U_y$ and the lateral projection of the buoyancy force $-\rho\vartheta g_y$. It is clearly seen in figure 4 that $[\mathbb{A}\cdot\mathrm{d}\boldsymbol{U}/\mathrm{d}t]_y$ is much weaker than the other three contributions, which results in small variations of the lateral velocity. The torque balance in the $z$-direction reveals a similar behaviour. More precisely, the restoring added-mass torque $U_y(\mathbb{A}\cdot\boldsymbol{U})_x - U_x(\mathbb{A}\cdot\boldsymbol{U})_y$ which results from both the geometrical anisotropy of the bubble and the existence of a non-zero transverse velocity almost balances the vortical

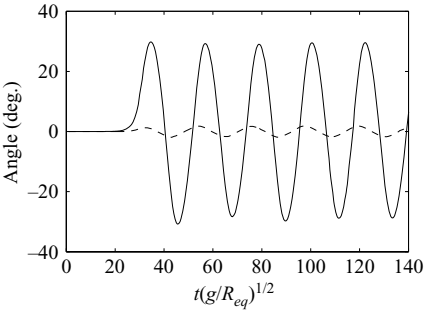


FIGURE 5. Evolution of the inclination angle with respect to the vertical (solid line) and of the drift angle $\beta$ (dashed line) during the zigzag.

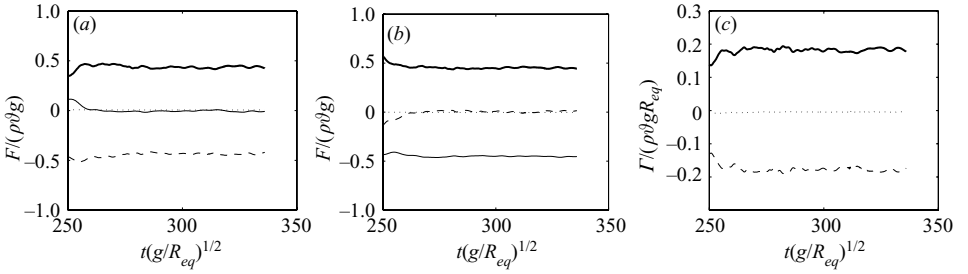


FIGURE 6. Lateral force and torque balances during the helical motion. (*a*) Force balance in the $y'$-direction ($y'$ is horizontal and points toward the centre of curvature of the trajectory); (*b*) force and (*c*) torque balance in the $z'$-direction (which points downward and is such that the $(x, z')$-plane is vertical). For meaning of line styles see figure 4.

torque $\Gamma_{\omega z}$. Hence the time rate-of-change term $[\mathbb{D}\cdot \mathrm{d}\boldsymbol{\Omega}/\mathrm{d}t]_z$ remains small along the whole path. Since the geometrical anisotropy of the bubble is large, so is the difference between the longitudinal and transverse components of $\mathbb{A}$. Therefore $U_y/U_x$ keeps small values, so that the direction of the bubble velocity remains close to that of the minor axis along the whole path. This is consistent with the experimental observations of Ellingsen & Risso (2001) who noticed that the drift angle $\beta = \tan^{-1}(U_y/U_x)$ was within the error bar of their optical measurements at all times. Here, as shown in figure 5, this angle is found to oscillate about zero with a maximum amplitude about 2°, the drift angle reaching its extrema close to the positions where the inclination angle is zero, i.e. close to the extremities of the zigzag. Coming back to the $y$-force balance, it is important to notice that the corresponding components of the buoyancy force and the centripetal added-mass force are 90° out of phase (see figure 4*b*), while $F_{\omega y}$ is shifted with respect to both of them. For instance, the transverse component of the buoyancy force reaches its extrema at the inflection point of the zigzag, while the centripetal added-mass force is zero there, owing to the vanishing of $\Omega_z$. This implies that the maximum inclination angle of the path, $\theta_{max}$, is determined by the value of the vortical force $F_{\omega y}$ at this moment. Similarly, $g_y$ vanishes at each extremity of the zigzag, leaving $F_{\omega y}$ and $\Omega_z(\mathbb{A}\cdot\boldsymbol{U})_x$ in balance. Therefore the maximum of the bubble rotation rate, $\Omega_{max}$, is determined by the corresponding value of $F_{\omega y}$.

To analyse the lateral force and torque balances during the helical stage, we project them onto the $(x, y', z')$ axes defined above, noting that the helix in figure 1 is clockwise and has a pitch angle close to 27°. As shown in figure 6, these balances follow straightforward evolutions once the trajectory becomes close to an exact circular helix ($t(g/R_{eq})^{1/2} > 270$). Again the vortical torque $\Gamma_{\omega z'}$ is essentially balanced

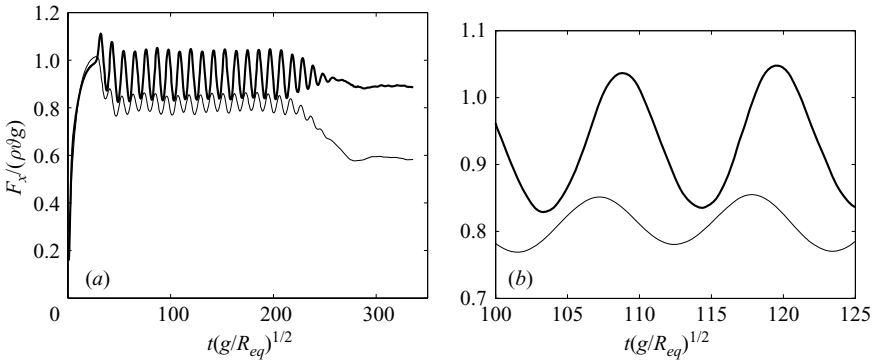


FIGURE 7. Compared evolutions of $\|F_{\omega x}\|$ and $\|F_s\|$ derived from Moore's (1965) prediction: (*a*) complete evolution; (*b*) zoom over one period of the zigzag. Thick line: computed drag $F_{\omega x}$; thin line: Moore's (1965) prediction $F_s$.

by the restoring added-mass torque which acts to maintain a small constant drift angle. The main difference with the zigzag is encountered in the lateral force balance, where buoyancy and added-mass effects now act in two perpendicular directions. More precisely, $F_{\omega y'}$ is centripetal and is essentially balanced by the centrifugal force $-\Omega_{z'}(\mathbb{A}\cdot\boldsymbol{U})_x$ while $F_{\omega z'}$ is balanced by the transverse component of the buoyancy force $-\rho\vartheta g_{z'}$. Hence the $y'$-force balance determines the rotation rate $\Omega_{z'}$ while the $z'$-balance determines the pitch angle $\theta$.

### 3.3. *Wake-induced drag*

It is of interest to compare the evolution of $F_{\omega x}$ with that of the drag $F_s$ the bubble would experience if its wake were axisymmetric. For this purpose, knowing the instantaneous bubble Reynolds number $Re = 2R_{eq}\|\boldsymbol{U}\|/\nu$, we evaluated $F_s(\chi, Re)$ using Moore's expression for the drag of an oblate bubble rising steadily at large Reynolds number (Moore 1965). The comparison is displayed in figure 7. During the zigzag and helical stages, $F_s$ has values consistently smaller than $F_{\omega x}$; the maximum value of the difference $\|F_{\omega x}\| - \|F_s\|$ is about $0.22\,\rho\vartheta g$ during the zigzag and increases to $0.3\rho\vartheta g$ in the helical stage. This difference may be thought of as an additional drag resulting from the 'sucking' of the bubble by its three-dimensional wake. More precisely, the cores of the two counter-rotating vortices are low-pressure regions which, compared to the axisymmetric situation, increase the pressure difference between the front and back regions of the bubble. During the zigzag, $F_{\omega x}$ and $F_s$ oscillate with the same frequency but are about 90° out of phase. Comparing figure 7(*b*) with figure 4(*b*) reveals that the minimum of $\|F_{\omega x}\| - \|F_s\|$ and the vanishing of $F_{\omega y}$ occur at the same instant and that both components of the vortical force reach their maxima simultaneously. This is a clear indication that, similar to the lateral force $F_{\omega y}$, the wake-induced drag is due to the three-dimensionality of the wake, whereas Moore's prediction $F_{\omega x} = F_s$ is almost recovered as soon as the wake recovers its axisymmetry.

## 4. Influence of the bubble kinematics on vortical effects

The material in the previous section allows us to better understand how the bubble–fluid system satisfies Newton's second law for a given evolution of the vortical force and torque along two- or three-dimensional trajectories with a given geometry. It may also provide insight into the way the variations of $\boldsymbol{U}$ and $\boldsymbol{\Omega}$ (which also includes those of the drift angle $\beta$) influence $\boldsymbol{F}_\omega$ and $\boldsymbol{\Gamma}_\omega$. More precisely, figure 8 makes it clear

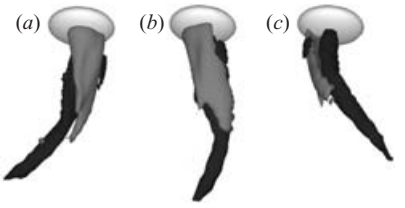


FIGURE 8. Evolution of the streamwise vorticity in the wake during the helical motion; (*a*) $t(g/R_{eq})^{1/2} = 310.9$; (*b*) a quarter of a period later; (*c*) half a period later.

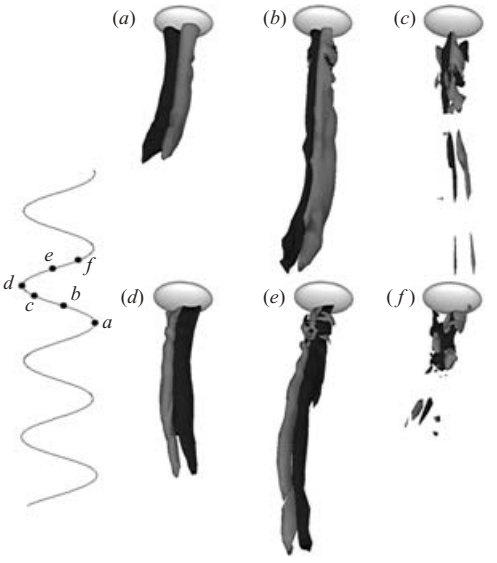


FIGURE 9. Evolution of the streamwise vorticity in the wake during one period of the zigzag.

that, from the beginning of the helical stage, the three-dimensional wake reaches a stationary structure. Figures 2 and 6 confirm that during this stage the wake delivers a constant force $\boldsymbol{F}_\omega$ and a constant torque $\boldsymbol{\Gamma}_\omega$ and that the corresponding balances are stationary in the appropriate system of axes. This allows us to conclude that, in the range of Reynolds number and aspect ratio considered here, the wake and the associated dynamical effects reach a steady state in presence of constant $\boldsymbol{U}$ and $\boldsymbol{\Omega}$. The question is then to better understand what happens during the zigzag motion where both quantities vary periodically. Figure 9 shows how the three-dimensional wake structure evolves during one period of the zigzag. The coupling between the variations of $\boldsymbol{U}$ and $\boldsymbol{\Omega}$ and the strength and sign of the two streamwise vortices is striking. This sign appears to be directly related to the rotation of the bubble which induces a slight asymmetry in the flow, with velocities larger on the side opposite the centre of curvature of the path. This asymmetry, which reaches its maximum at each extremity of the zigzag, results in a maximum velocity difference about $0.1U_x$ between the two opposite sides of the bubble. While small, this difference turns out to be sufficient to drive the sign of the streamwise vortices. Note however that there is a significant time delay (about $3.5(R_{eq}/g)^{1/2}$ according to figure 4, i.e. $10R_{eq}/U_x$) between the vanishing of $\Omega_z$ at the inflection points of the path (points $b$ and $e$ in figure 9) and the change of sign of the trailing vortices near points $c$ and $f$. The variations of $\boldsymbol{U}$ and $\boldsymbol{\Omega}$ may also be evaluated to obtain the magnitude of the accelerations undergone by the bubble. It turns out that the relative variation of $U_x$ between the extremity and the inflection point of the path

is about 10 %, which results in a maximum acceleration $|\mathrm{d}U_x/\mathrm{d}t|$ (reached midway between the extremity and the inflection point of the zigzag) about $0.09g$. The transverse acceleration $|\mathrm{d}U_y/\mathrm{d}t|$ and the angular acceleration $R_{eq}|\mathrm{d}\Omega_z/\mathrm{d}t|$ (both reached at the inflection point) are about $0.03g$ and $0.05g$, respectively. The corresponding decrease (resp. increase) in the bubble velocity from $a$ to $b$ and $d$ to $e$ in figure 9 (resp. from $b$ to $d$ and from $e$ to the next point $a$) are associated with dramatic changes in the wake structure. More precisely, figure 4($b$) indicates that $F_{\omega y}$ vanishes approximately midway between each inflection point and the next extremity of the zigzag (points $c$ and $f$ in figure 9), i.e. this vanishing almost coincides with the maximum of the streamwise acceleration. Similarly, the maximum of $|F_{\omega y}|$ occurs midway between the extremity of the zigzag and the inflection point, i.e. it coincides with the maximum of the streamwise deceleration. In other words $|F_{\omega y}|$ decreases from its maximum to zero during the part of the motion where $\mathrm{d}^2U_x/\mathrm{d}t^2$ is positive and then grows from zero to this maximum when $\mathrm{d}^2U_x/\mathrm{d}t^2$ is negative. Figures 4 and 9 also make it clear that the vanishing of $F_{\omega y}$ almost coincides with that of the streamwise vortices (i.e. it happens close to points $c$ and $f$), while $|F_{\omega y}|$ reaches its maximum when the intensity of the vortices in the near wake is the strongest (which occurs in between points $a$ and $b$ or $d$ and $e$, as indicated by the diameter of the vortices just at the rear of the bubble).

While at present qualitative, the above observations show that the wake dynamics are extremely sensitive to the changes in $\boldsymbol{U}$ and $\boldsymbol{\Omega}$, as the changes of sign of $\Omega_z$ combined with modest levels of velocity variations and acceleration turn out to be capable of forcing the three-dimensional wake structure to disappear and then reappear following a non-intuitive evolution. Detailed numerical investigations with imposed evolutions of $\boldsymbol{U}(t)$ and $\boldsymbol{\Omega}(t)$ are required to explore this sensitivity in more detail and open the route toward rational low-dimensional models of $\boldsymbol{F}_\omega(t)$ and $\boldsymbol{\Gamma}_\omega(t)$.

## REFERENCES


Ellingsen, K. & Risso, F. 2001 On the rise of an ellipsoidal bubble in water: oscillatory paths and liquid-induced velocity. *J. Fluid Mech.* **440**, 235–268.

Howe, M. S. 1995 On the force and moment on a body in an incompressible fluid, with application to rigid bodies and bubbles at low and high Reynolds numbers. *Q. J. Mech. Appl. Maths* **48**, 401–426.

Jenny, M., Dusek, J. & Bouchet, G. 2004 Instabilities and transition of a sphere falling or ascending freely in a Newtonian fluid. *J. Fluid Mech.* **508**, 201–239.

Lamb, H. 1945 *Hydrodynamics*, 6th edn. Dover.

Magnaudet, J. & Eames, I. 2000 The motion of high-Reynolds-number bubbles in inhomogeneous flows. *Annu. Rev. Fluid Mech.* **32**, 659–708.

Magnaudet, J. & Mougin, G. 2006 Wake instability of a fixed spheroidal bubble. *J. Fluid Mech.* **in press**.

Moore, D. W. 1965 The velocity of rise of distorted gas bubbles in a liquid of small viscosity. *J. Fluid Mech.* **23**, 749–766.

Mougin, G. & Magnaudet, J. 2002*a* Path instability of a rising bubble. *Phys. Rev. Lett.* **88**, 14502 (referred to herein as MM).

Mougin, G. & Magnaudet, J. 2002*b* The generalized Kirchhoff equations and their application to the interaction between a rigid body and an arbitrary time-dependent viscous flow. *Intl J. Multiphase flow* **28**, 1837–1851.

Prosperetti, A., Ohl, C. D., Tijink, A., Mougin, G. & Magnaudet, J. 2003 Leonardo's paradox. Appendix to A. Prosperetti, C. D. Ohl & A. Tijink. *J. Fluid Mech.* **482**, 296–299.

Quartapelle, L. & Napolitano, M. 1983 Force and moment in incompressible flows. *AIAA J.* **21**, 911–913.

Wu, J. C. 1981 Theory for aerodynamic force and moment in viscous flows. *AIAA J.* **19**, 432–441.